Gate-controlled reversible rectifying behavior investigated in a two-dimensional MoS$_2$ diode

Qian Liu,[1] Jia-Jin Li,[1] Dan Wu,[1] Xiao-Qing Deng,[1] Zhen-Hua Zhang,[1] Zhi-Qiang Fan ●,[1,*] and Ke-Qiu Chen[2,†]

[1]*Hunan Provincial Key Laboratory of Flexible Electronic Materials Genome Engineering, School of Physics and Electronic Science,*
Changsha University of Science and Technology, Changsha 410114, China
[2]*Department of Applied Physics, School of Physics and Electronics, Hunan University, Changsha 410082, China*

By using density functional theory and *ab initio* quantum-transport simulation, we study the Schottky barrier and the rectifying behavior of diodes consisting of the two-dimensional metal phase 1*T*-MoS$_2$ and semiconductor phase 2*H*-MoS$_2$. The results show that the Schottky barrier of the out-of-plane (OP) contacted MoS$_2$ heterostructure diode is a little different from that of the in-plane (IP) contacted MoS$_2$ heterostructure diode. The current-voltage characteristics show that the OP diode has the better rectifying behavior compared to the IP diode under the zero gate voltage. The corresponding maximum rectifier ratio of the OP Schottky barrier diode is close to 10^7 at 0.9 V bias voltage. More interestingly, we find that the gate voltage can be used to effectively control the rectifying behavior of the two diodes. The positive gate voltages can increase the current value of two Schottky barrier diodes, but weaken their rectification ratios. The negative gate voltages can reverse the rectifying direction of two Schottky barrier diodes. The above results provide good theoretical guidance for the designing of diode devices based on two-dimensional materials in the future.

I. INTRODUCTION

Today, new materials and technologies have become a research hot spot in the post-Moore era; they are used to replace the traditional silicon-based materials, thus extending Moore's law to the nanoscale where quantum transport plays a leading role [1,2]. In order to improve the performance of silicon-based semiconductor devices, academic researchers have been turning out fin field effect transistors (FETsT), negative capacitance FETs, and other exotic-shaped devices for years [3–5]. At the same time, academic researchers have also proposed a variety of "more than Moore" devices, such as molecular devices [6–9], optoelectronic devices [10,11], spintronic devices [12–14], and thermoelectric devices [15,16]. Although these imaginative researchers have achieved significant results, it is still difficult to subvert the traditional silicon-based semiconductor devices in a short time. As semiconductors struggle on the tiny scale of today's devices, academic researchers are forced to consider other materials. Low-dimensional materials, especially two-dimensional (2D) layered materials, have attracted extensive research interest due to their novel physical and chemical properties and potential applications in electronic applications in the postsilicon era [17–20]. Currently, the use of silicene [21], phosphorene [22–25], borophene [26], MXene [27], transition metal sulfides (TMDs) [28–31], and other 2D materials to design and manufacture nanoscale functional electronic devices has become an important research direction all over the world [32–36]. The research results of FETs based on 2D materials are gradually increasing, which provides a new solution for the current silicon-based semiconductor industry [37,38].

Among 2D materials with potential novel properties, TMDs have gained extensive attention due to useful physicochemical properties and have revealed broad potential applications [39–42]. Generally, based on the arrangement of sulfur atoms, monolayer TMDs show diverse structures, including *H*-phase and *T* (or *T'*) phases with different symmetry, and have different electronic structure properties [43–46]. Heterostructures of 2D TMDs have attracted enormous interest as they display unique functionalities and have the potential to be applied in next-generation electronics. Based on their changeable electronic properties, the heterojunctions of 2D TMDs with different phases have been fabricated with the help of mechanical strain and chemical modification to form low-resistance contact FETs [47–51]. However, a detailed study to investigate the Schottky barrier (SB) and the rectifying behavior of diodes consisting of the 2D TMDs with different phases has not been fully developed. Diodes are used for various applications, ranging from power conversion to overvoltage protection and from signal detection and mixing to switches. Consequently, in this work, the out-of-plane (OP) and in-plane (IP) contacted MoS$_2$ heterostructure diodes are examined theoretically by using the first-principle method of nonequilibrium Green's function (NEGF) based on density functional theory (DFT). Furthermore, it has been reported that gate voltage is one of the important ways to control SB and then influence diode rectification [52–55]. Hence, dual-gated MoS$_2$ heterostructure diodes are also constructed to explore the modulation of the gate voltage on their rectifying behavior.

II. MODEL AND SIMULATION APPROACH

The OP and IP contacted MoS$_2$ heterostructure diodes are shown schematically in Figs. 1(a) and 1(c). The blue dashed

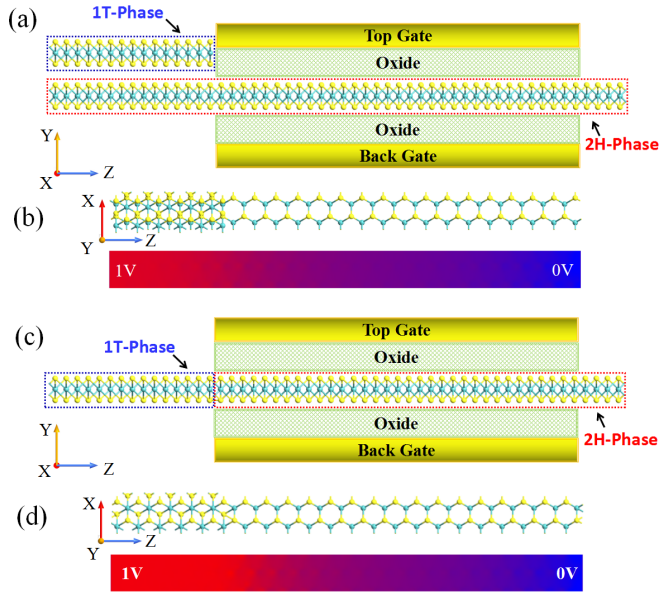*zqfan@csust.edu.cn
†keqiuchen@hnu.edu.cn

FIG. 1. Schematic diagrams of (a) OP and (c) IP contacted MoS$_2$ heterostructure diodes. The corresponding voltage drop diagrams of (b) OP and (d) IP contacted MoS$_2$ heterostructure diodes.
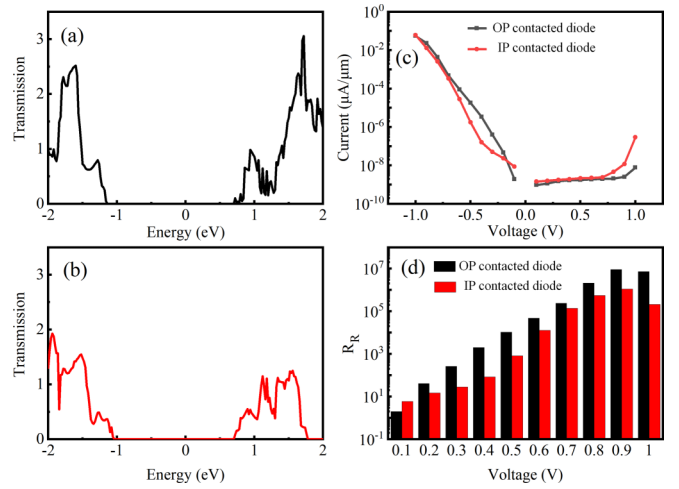

FIG. 2. Transmission spectra of (a) OP and (b) IP contacted MoS$_2$ heterostructure diodes under zero bias without gate voltage. Fermi level is set to zero in the energy scale. (c) Current-voltage characteristics of two heterostructure diodes without gate voltage. (d) The corresponding rectification ratios of two heterostructure diodes in the bias region from 0.1 to 1.0 V.

line frames are the metal phase 1T-MoS$_2$ and the red dashed line frames are the semiconductor phase 2H-MoS$_2$, which are considered as the central regions of the heterostructure diodes. The left and right regions outside of the central regions are two electrodes. The effective oxide thickness (EOT) of each dielectric region above or below the semiconductor phase 2H-MoS$_2$ is 0.41 nm. The corresponding dielectric constant is 3.9. Here, EOT indicates how thick a silicon oxide film would need to be to produce the same effect as the high-k material being used. The yellow regions above and below the oxide layers are the top and back gates, which provide the gate voltage on the semiconductor phase 2H-MoS$_2$. The length of the gate is 5.1 nm. A vacuum layer of 15 Å is selected in two directions perpendicular to the electron transport to shield the periodic nearest neighbor interaction. Figures 1(b) and 1(d) show the total voltage drop of 1.0 V across the OP and IP contacted MoS$_2$ heterostructure diodes. A drop in voltage corresponds to a quantum resistance, and this explains the observed finite-bias splitting of the zero-bias resonance [56,57]. It is clear from both figures that most of the voltage drop takes place around the central regions, not in the electrodes. Therefore, the potential in the central region converges smoothly towards the electrode potentials, such that there is no scattering at the two electrode-central region interfaces.

The geometric optimization and electron transport properties in this work are carried out by using the first-principle software package ATOMISTIX TOOLKIT, which is based on DFT in combination with the NEGF [58]. The exchange and correlations were described by the Perdew-Burke-Ernzerhof (PBE) functional under the generalized gradient approximation (GGA). The k-point samplings for calculations of the electronic transport properties of the OP and IP contacted MoS$_2$ heterostructure diodes are $12 \times 1 \times 100$, respectively. When a bias voltage is applied, the current through the junction is calculated by using the Landauer formula, $I(V_b) =$

$(\frac{2e}{h}) \int_{\mu_L}^{\mu_R} (f_L - f_R) T(E, V_b) dE$ [59], where $\mu_{L/R}$ is the electrochemical potentials of the left and right electrodes, $f_{L/R}$ is the Fermi distribution function. The transport coefficient $T(E, V_b)$ can be calculated using the well-known formula $T(E, V_b) = \mathrm{Tr}[\Gamma_L(E) G^R(E) \Gamma_R(E) G^A(E)]$, where $G^R(E)$ and $G^A(E)$ are the retarded and advanced Green's functions, respectively.

III. RESULTS AND DISCUSSIONS

Figures 2(a) and 2(b) depict the transmission spectra of the OP and IP contacted MoS$_2$ heterostructure diodes under the zero bias without gate voltage. As shown, there are two identical transmission forbidden regions in the electronic transmission spectra of two heterostructure diodes. The width of the forbidden region is 1.8 eV, which is consistent with the energy band gap of MoS$_2$ [39–42]. In addition, the highest transmission coefficient of the OP contacted MoS$_2$ heterostructure diode is greater than 3, while that of the IP contacted MoS$_2$ heterostructure diode is less than 2. The hole Schottky-barrier height (SBH) can be extracted by measuring the energy difference between the Fermi level (FL) of 1T-phase MoS$_2$ and the valence band maximum (VBM) of the MoS$_2$ in the transmission spectrum. The energy difference between the FL of 1T-phase MoS$_2$ and the VBM of the MoS$_2$ in Fig. 2(a) is larger than that in Fig. 2(b), so the OP contacted MoS$_2$ heterostructure diode has a larger hole SBH than that of the IP contacted MoS$_2$ heterostructure diode.

The current-voltage characteristics of two heterostructure diodes without gate voltage can be calculated by the Landauer formula as shown in Fig. 2(c). The current values here are all absolute values in order to draw the logarithmic diagram. One can find that the currents of the OP and IP contacted MoS$_2$ heterostructure diodes will increase rapidly with the negative bias. However, the corresponding currents hardly increase with the increase of positive bias before 0.9 V (0.7 V) for the OP (IP) contacted MoS$_2$ heterostructure diode. Therefore, the
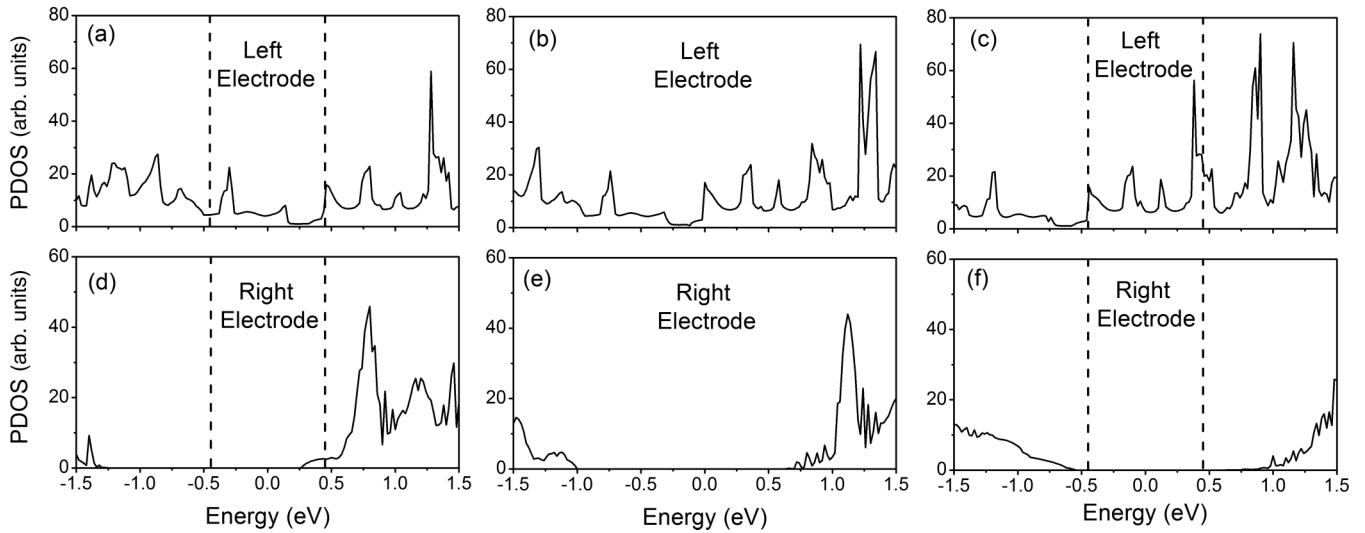
FIG. 3. (a)–(c) PDOS of left electrode for the OP contacted MoS$_2$ heterostructure diode under –0.9, 0.0, and 0.9 V bias. (d)–(f) PDOS of right electrode for the OP contacted MoS$_2$ heterostructure diode under –0.9, 0.0, and 0.9 V bias. The region between the two dashed lines is the bias window.

current-voltage characteristics of two heterostructure diodes all present the obvious rectifying behavior. In order to explore the rectifying performance clearly, we report the rectification ratios of two heterostructure diodes in Fig. 2(d). Here, the rectification ratio (R_R) is the ratio of the current of the negative bias to the current of the positive bias one, $R_R(V) = I(-V)/I(+V)$ [60]. From the figure, one can find that the R_R of two heterostructure diodes will increase gradually with the bias first, then decrease after 0.9 V due to the increasing of the positive currents. In addition, the R_R of the OP contacted MoS$_2$ heterostructure diode are always bigger than those of the IP contacted MoS$_2$ heterostructure diode after 0.1 V. The OP and IP contacted MoS$_2$ heterostructure diodes all perform the maximal R_R 10^7 and 10^6 at 0.9 V, respectively. It indicates that the OP contacted MoS$_2$ heterostructure diode has the better rectifying performance than that of the IP contacted MoS$_2$ heterostructure diode.

To understand the obvious rectifying behavior of the OP contacted MoS$_2$ heterostructure diode, we show its projected density of states (PDOS) of the left and right electrodes under −0.9, 0.0, and 0.9 V bias voltages in Fig. 3. Under the zero-bias voltage, the PDOS spectrum of the left electrode consists of a series of peaks due to the metallicity of the 1T-MoS$_2$, as shown in Fig. 3(b). Because the 2H-MoS$_2$ in the right electrode is a semiconductor, there is a large energy region (about 1.8 eV) in the PDOS spectrum in Fig. 3(e), and its coefficient is zero. After the negative bias is applied, the PDOS spectra of the left or the right electrodes will shift to right or left relative to FL, respectively. In Fig. 3(a), there is a series of PDOS peaks distributing in the energy region from −1.5 to 1.5 eV. In Fig. 3(d), the partial conduction band minimum (CBM) of the semiconductor phase 2H-MoS$_2$ (the right electrode) moves into the bias window when the bias voltage increases to −0.9 V. As a result, the PDOS of the right electrode can match with the PDOS of the left electrode in the bias window, leading to the big current. After the positive bias is applied, the PDOS of the left or right electrode will shift to left or right relative to FL, respectively. In Fig. 3(c),

there are also a series of PDOS peaks distributing in the bias window, which are higher than that in Fig. 3(a). When the bias voltage increases to 0.9 V, the coefficient in the bias window is still zero despite the shift of the PDOS spectrum, as shown in Fig. 3(f). Therefore, the PDOS of the left and right electrodes do not match each other in the bias window, resulting in a very small current passing through the device. As a result, the OP contacted MoS$_2$ heterostructure diode presents an obvious rectifying behavior. When the positive bias voltage further increases, the VBM of the semiconductor phase 2H-MoS$_2$ (the right electrode) will move into the bias window leading to the rapid increasing of current. Then, the rectifying behavior will be weakened with the decrease of corresponding R_R.

The zero-bias transmission spectra of the dual-gated OP and IP contacted MoS$_2$ heterostructure diodes under 0.25, 0.5, 0.75 V gate voltages and −0.25, −0.5, −0.75 V gate voltages can be seen in Fig. 4. For the dual-gated OP and IP contacted MoS$_2$ heterostructure diodes, the right edges of the transmission forbidden regions still hold on the same energy, but the transmission coefficients will decrease gradually while the positive gate voltages increasing, as shown in Figs. 4(a) and 4(b). However, the left edges of the transmission forbidden regions will shift far away from the FL with the increasing of the positive gate voltage leading to the widening of the transmission forbidden regions. In addition, the transmission coefficients also decrease obviously while the positive gate voltages increase. When the negative gate voltages are applied, the left edges of the transmission forbidden regions always hold on the same energy for the dual-gated OP and IP contacted MoS$_2$ heterostructure diodes. However, the right edges of the transmission forbidden regions will shift far away from the FL with the increasing of the negative gate voltage also leading to the widening of the transmission forbidden region, as shown in Figs. 4(c) and 4(d). In addition, the transmission coefficients also decrease obviously with the increasing of the negative gate voltages. Thus, the obvious changes of the transmission spectra with the positive and negative gate voltages will greatly affect the
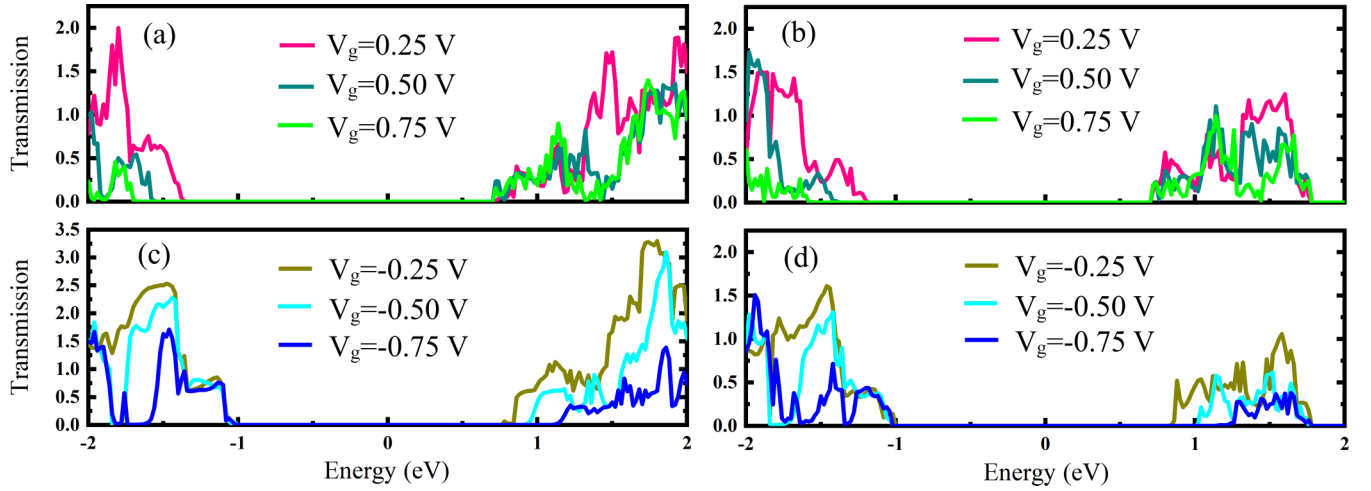
FIG. 4. Zero-bias transmission spectra of the dual-gated (a) OP and (b) IP contacted MoS$_2$ heterostructure diodes under 0.25, 0.5, and 0.75 V gate voltages, respectively. Zero-bias transmission spectra of the dual-gated (c) OP and (d) IP contacted MoS$_2$ heterostructure diodes under -0.25, -0.5, and -0.75 V gate voltages, respectively. Fermi level is set to zero in the energy scale.
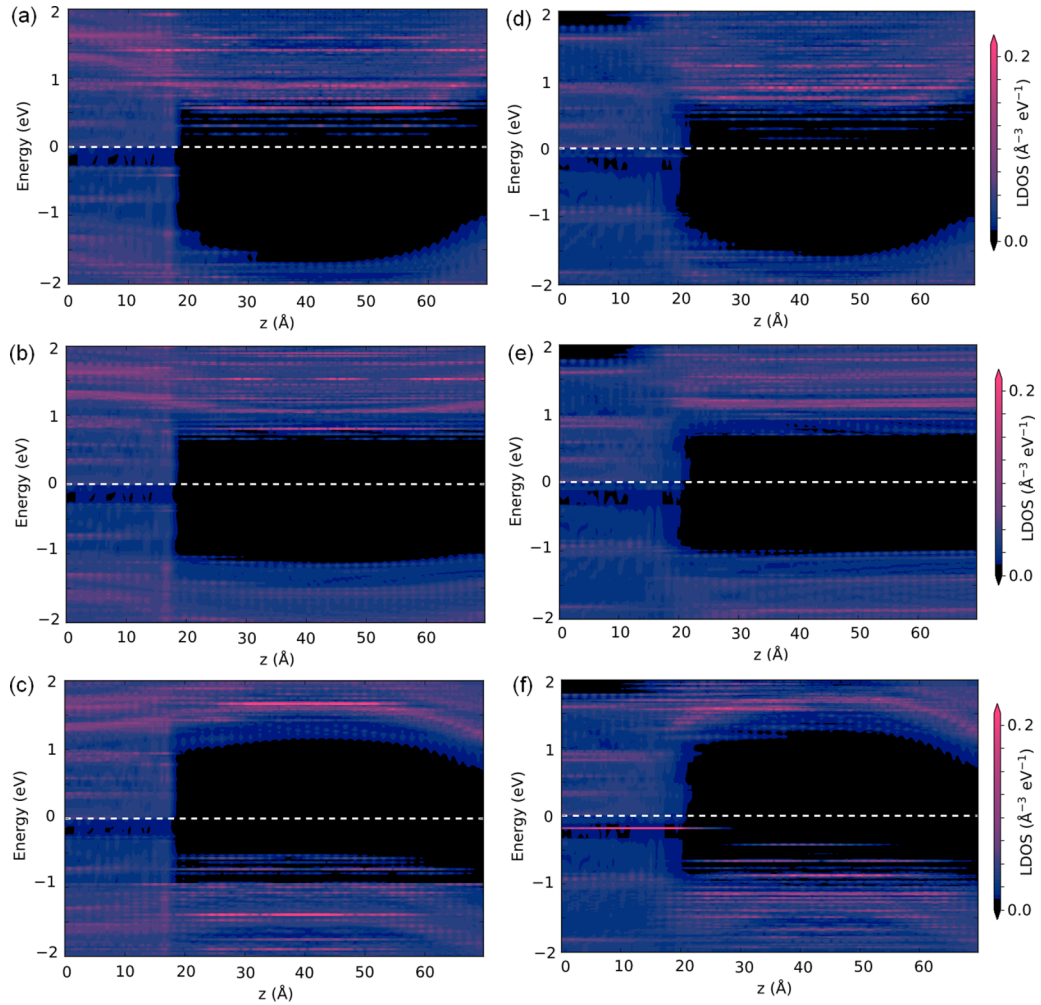

FIG. 5. Zero-bias LDOS of the dual-gated OP contacted MoS$_2$ heterostructure diode under (a) 0.75 V, (b) 0.0 V, and (c) -0.75 V gate voltages, respectively. The zero-bias LDOS of the dual-gated IP contacted MoS$_2$ heterostructure diode under (d) 0.75 V, (e) 0.0 V, and (f) -0.75 V gate voltages, respectively. Fermi level is set to zero in the energy scale.
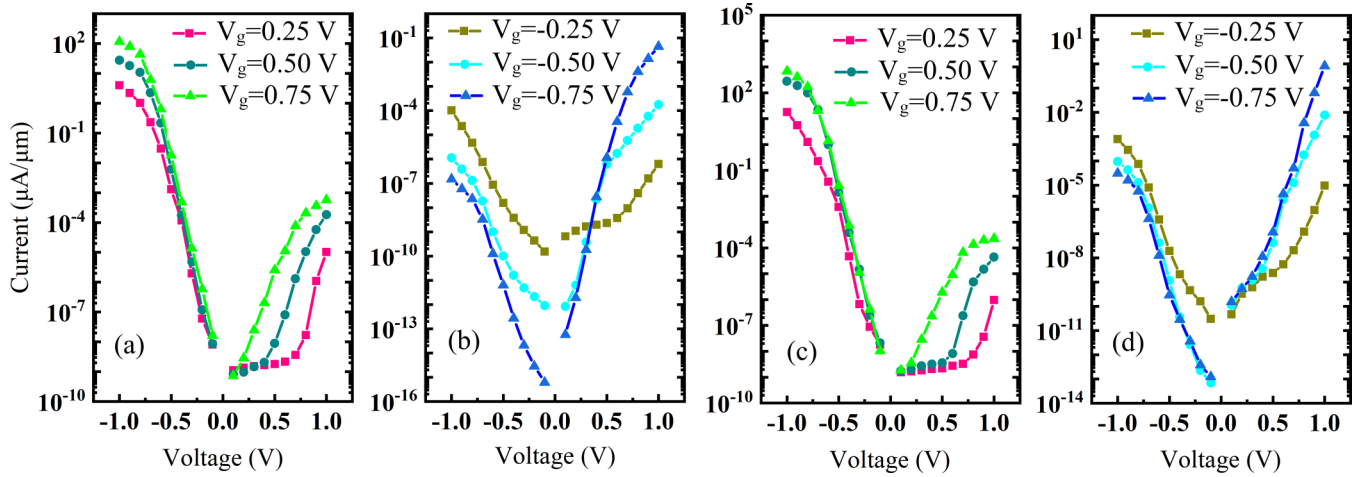
FIG. 6. Current-voltage characteristics of the dual-gated OP contacted MoS$_2$ heterostructure diode under 0.25, 0.5, 0.75 V gate voltages (a) and -0.25, -0.5, -0.75 V gate voltages (b), respectively. Current-voltage characteristics of the dual-gated IP contacted MoS$_2$ heterostructure diode under 0.25, 0.5, 0.75 V gate voltages (c) and -0.25, -0.5, -0.75 V gate voltages (d), respectively.

transport properties of the device resulting in the modulation of its rectifying behavior.

In order to understand the changes of the transmission spectra, we plot the projected local density of states (LDOS) of the dual-gated OP and IP contacted MoS$_2$ heterostructure diodes under 0.75, 0.0, and -0.75 V gate voltages in Fig. 5. The projected LDOS offers a highly useful visualization of the band diagram of the interface between the metal phase 1T-MoS$_2$ and the semiconductor phase 2H-MoS$_2$. The projected LDOS shows a high DOS in the metal phase 1T-MoS$_2$ (pink regions), while the black regions correspond to vanishing DOS in the band gap of the semiconductor phase 2H-MoS$_2$. Under zero gate voltage, the bands are essentially flat and the FLs of the metal phase 1T-MoS$_2$ locate within the band gaps of the semiconductor phase 2H-MoS$_2$, as shown in Figs. 5(b) and 5(e). Under 0.75 V gate voltage, there is the obvious downward band bending of the central semiconductor

phase 2H-MoS$_2$, as shown in Figs. 5(a) and 5(d). As a result, the left edges of the transmission forbidden regions shift far away from the FL leading to the widening of the transmission forbidden regions for two devices. Under -0.75 V gate voltage, there is the obvious upward band bending of the central semiconductor phase 2H-MoS$_2$, as shown in Figs. 5(c) and 5(f). Therefore the right edges of the transmission forbidden regions shift far away from the FL, also leading to the widening of the transmission forbidden regions for two devices. In addition, the band bending all leads to the decrease of transmission coefficients near the VMB and CBM of the central semiconductor phase 2H-MoS$_2$.

Current-voltage characteristics of the dual-gated OP and IP contacted MoS$_2$ heterostructure diodes under 0.25, 0.5, 0.75 V gate voltages and -0.25, -0.5, -0.75 V gate voltages are shown in Fig. 6. From Figs. 6(a) and 6(c), one can find that the current values of two diodes in the negative bias region will
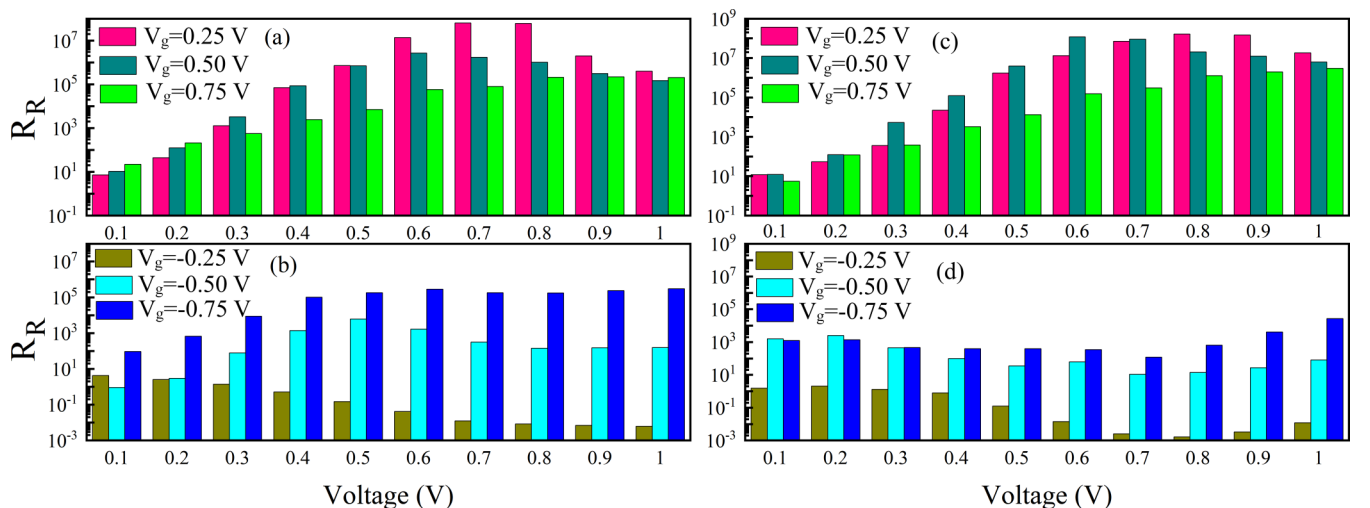

FIG. 7. Rectification ratios of the dual-gated OP contacted MoS$_2$ heterostructure diode under 0.25, 0.5, 0.75 V gate voltages (a) and -0.25, -0.5, -0.75 V gate voltages (b), respectively. Rectification ratios of the dual-gated IP contacted MoS$_2$ heterostructure diode under 0.25, 0.5, 0.75 V gate voltages (c) and -0.25, -0.5, -0.75 V gate voltages (d), respectively.
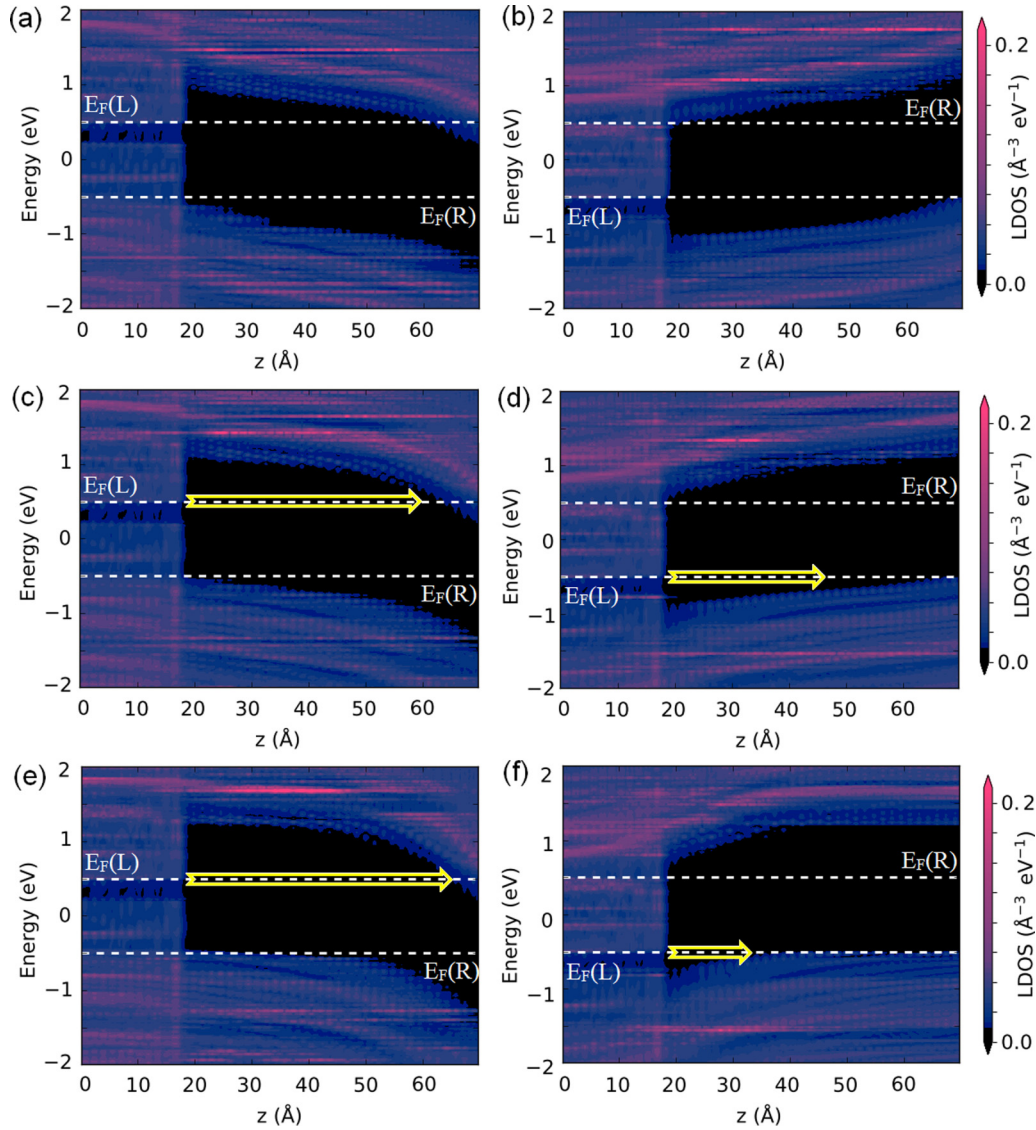
FIG. 8. LDOS of the dual-gated OP contacted MoS_2 heterostructure diode, left electrode at -1.0 V (a) and 1.0 V (b) bias voltage under -0.25 V gate voltage. LDOS of the dual-gated OP contacted MoS_2 heterostructure diode, left electrode at -1.0 V (c) and 1.0 V (d) bias voltage under -0.5 V gate voltage. LDOS of the dual-gated OP contacted MoS_2 heterostructure diode left electrode at -1.0 V (e) and 1.0 V (f) bias voltage under -0.75 V gate voltage. $E_F(L)$ and $E_F(R)$ are the Fermi levels of the left and right electrode, respectively.

increase slowly under the positive gate voltage. However, the current values of two diodes in the positive bias region will be greatly improved. Especially when the gate voltage is 0.75 V, the currents increase linearly with the positive voltage. The currents in the negative bias region are still bigger than those in the positive bias region, so the current-voltage character- istics of two heterostructure diodes all present the rectifying behavior and the rectifying directions are the same as that at zero gate voltage. In Figs. 6(b) and 6(d), one can find that the current values of two diodes in the negative bias region will decrease rapidly under the negative gate voltage. However, the current values of two diodes in the positive bias region will be greatly improved. Especially when the gate voltages are -0.5 and -0.75 V, the currents increase linearly with the positive voltage. As a result, the currents of two diodes in the negative bias region are less than those in the positive bias region. The rectifying directions under the -0.5 and -0.75

V gate voltages are opposite compared with that of the zero gate voltage. In other words, the gate voltage can be employed as an important way to modulate the rectifying behavior of the OP and IP contacted MoS_2 heterostructure diodes in this paper.

To further characterize the adjustable rectifying behavior, we calculate the rectification ratios of the OP and IP contacted MoS_2 heterostructure diodes under the different gate voltages in Fig. 7. In Figs. 7(a) and 7(c), the R_R is the ratio of the current of the negative bias to the current of the positive bias one, $R_R(V) = I(-V)/I(+V)$. When the gate voltage is 0.25 V, the maximal R_R of the OP contacted MoS_2 heterostructure diode is up to the magnitude of 10^8, which has an order of magnitude improvement compared with that of the zero gate voltage. However, further increasing the positive gate voltage will reduce the R_R as shown in Fig. 7(a). For the IP contacted MoS_2 heterostructure diode, the positive gate voltage also

enhances the R_R first, then reduces it. When the gate voltage is 0.5 V, the maximal R_R is up to the magnitude of 10^8 as shown in Fig. 7(c), which has two orders of magnitude improvement compared with that of the zero gate voltage. In Figs. 7(b) and 7(d), the R_R is the ratio of the current of the positive bias to the current of the negative bias one, $R_R(V) = I(+V)/I(-V)$. From the figure, one can find that the R_R's of two heterostructure diodes are very small under the -0.25 V gate voltage. Further increasing of the negative gate voltage will enlarge the R_R of the two diodes. The R_R of the OP contacted MoS$_2$ heterostructure diode exceeds 10^5 at 0.4 V and continues steadily to 1 V under -0.75 V gate voltage, as shown in Fig. 7(b). As is widely known, being a stable rectifier is also an important property of the diode. In Fig. 7(d), further increasing of the negative gate voltage does not significantly improve the rectifying behavior of the IP contacted MoS$_2$ heterostructure diode. Moreover, the corresponding R_R fluctuates greatly in the entire bias range, which greatly affects its application.

Figure 8 shows the projected LDOS of the dual-gated OP contacted MoS$_2$ heterostructure diode at -1.0 and 1.0 V bias voltages under -0.25, -0.5, and -0.75 V gate voltages, which can help us understand the reversal of rectifier direction caused by negative gate voltage. In Figs. 8(a) and 8(b), the upward band bending of the central semiconductor phase 2H-MoS$_2$ induced by negative gate voltage weakens the electron tunneling from the left electrode to the right electrode at -1.0 V bias voltage, but enhances the electron tunneling from the left electrode to the right electrode at 1.0 V bias voltage. Therefore, the rectifying behavior of the dual-gated OP contacted MoS$_2$ heterostructure diode under -0.25 V gate voltage will be weakened, as shown in Fig. 6(b). The greater upward band bending of the central semiconductor phase 2H-MoS$_2$ induced by the further increase of the negative gate voltage would extend or reduce the tunneling lengths around the $E_F(L)$, as shown in Figs. 8(c) and 8(d) by yellow arrows. As a result, the current at 1.0 V bias voltage is larger than that at -1.0 V bias voltage under -0.5 V gate voltage. The rectifying direction of the diode is opposite compared with that of the zero gate voltage. In Figs. 8(e) and 8(f), the tunneling lengths around the $E_F(L)$ will be further extended or reduced at -1.0 or 1.0 V bias voltages due to the continued upward band bending of the central semiconductor phase 2H-MoS$_2$. As a result, the reversed rectifying behavior of the diode is enhanced under -0.75 V gate voltage.

IV. CONCLUSION

In this paper, we study the Schottky barrier and the rectifying behavior of diodes consisting of the two-dimensional metal phase 1T-MoS$_2$ and semiconductor phase 2H-MoS$_2$ by using an *ab initio* quantum-transport simulation method based on density functional theory and the nonequilibrium Green's function. The results show that the Schottky barrier of the out-of-plane (OP) contacted MoS$_2$ heterostructure diode is a little different from that of the in-plane (IP) contacted MoS$_2$ heterostructure diode. The current-voltage characteristics show that the OP diode has the better rectifying behavior compared to the IP diode under the zero gate voltage. The corresponding maximum rectifier ratio of the OP Schottky barrier diode is close to 10^7 at 0.9 V bias voltage. More importantly, the downward and upward band bending of the central semiconductor phase 2H-MoS$_2$ induced by the positive and negative gate voltages can extend the width of the transmission forbidden region of two diodes and modulate the corresponding rectifying behavior. Positive gate voltages can increase the current value of the two diodes, but weaken their rectification ratios. Negative gate voltages can change the tunneling lengths around the $E_F(L)$ and reverse the rectifying direction of the two diodes. The reversed rectifying behavior of the two diodes can be enhanced while the negative gate voltage increases.

[1] K. Y. Jeong, M. S. Hwang, J. Kim, J. S. Park, J. M. Lee, and H. G. Park, Adv. Mater. **32**, 2001996 (2020).

[2] Y. Cui, B. Li, J. B. Li, and Z. M. Wei, Sci. China: Phys. Mech. Astron. **61**, 016801 (2018).

[3] S. Salahuddin and S. Datta, Nano Lett. **8**, 405 (2008).

[4] K. Tomioka, M. Yoshimura, and T. Fukui, Nature **488**, 189 (2012).

[5] L. M. Peng, Z. Y. Zhang, and C. G. Qiu, Nat. Electron. **2**, 499 (2019).

[6] Z. Q. Fan, K. Q. Chen, Q. Wan, B. S. Zou, W. H. Duan, and Z. Shuai, Appl. Phys. Lett. **92**, 263304 (2008).

[7] D. Xiang, X. L. Wang, C. C. Jia, T. Lee, and X. F. Guo, Chem. Rev. **116**, 4318 (2016).

[8] Z. Q. Fan, Z. H. Zhang, W. Tian, X. Q. Deng, G. P. Tang, and F. Xie, Org. Electron. **14**, 2705 (2013).

[9] W. Y. Sun, X. Q. Cui, Z. Q. Fan, L. Y. Nie, and Z. H. Zhang, J. Phys. D: Appl. Phys. **52**, 155102 (2019).

[10] Y. Cui, Z. Q. Zhou, T. Li, K. Y. Wang, J. B. Li, and Z. M. Wei, Adv. Funct. Mater. **29**, 1900040 (2019).

[11] C. G. Zhao and L. Duan, J. Mater. Chem. C **8**, 803 (2020).

[12] W. Han, R. K. Kawakami, M. Gmitra, and J. Fabian, Nat. Nanotechnol. **9**, 794 (2014).

[13] Z. Zhu, Z. H. Zhang, D. Wang, X. Q. Deng, Z. Q. Fan, and G. P. Tang, J. Mater. Chem. C **3**, 9657 (2015).

[14] Z. Q. Fan, F. Xie, X. W. Jiang, Z. M. Wei, and S. S. Li, Carbon **110**, 200 (2016).

[15] D. Wu, X. H. Cao, S. Z. Chen, Y. X. Feng, L. M. Tang, W. X. Zhou, and K. Q. Chen, J. Mater. Chem. A **7**, 19037 (2019).

[16] D. Wu, X. H. Cao, P. Z. Jia, Y. J. Zeng, Y. X. Feng, L. M. Tang, W. X. Zhou, and K. Q. Chen, Sci. China: Phys. Mech. Astron. **63**, 276811 (2020).

[17] N. Li, Q. Q. Wang, C. Shen, Z. Wei, H. Yu, J. Zhao, X. B. Lu, G. L. Wang, C. L. He, L. Xie, J. Q. Zhu, L. J. Du, R. Yang, D. X. Shi, and G. Y. Zhang, Nat. Electron. **3**, 711 (2020).

[18] H. Yang, L. F. Pan, M. Q. Xiao, J. Z. Fang, Y. Cui, and Z. M. Wei, Sci. China Mater. **63**, 421 (2020).

[19] Y. Liu, Y. Huang, and X. F. Duan, Nature **567**, 323 (2019).

[20] Y. Ren, X. Y. Zhou, and G. H. Zhou, Phys. Rev. B **103**, 045405 (2021).

[21] P. Vogt, P. De Padova, C. Quaresima, J. Avila, E. Frantzeskakis, M. C. Asensio, A. Resta, B. Ealet, and G. Le Lay, Phys. Rev. Lett. **108**, 155501 (2012).

[22] Z. Q. Fan, W. Y. Sun, X. W. Jiang, J. W. Luo, and S. S. Li, Org. Electron. **44**, 20 (2017).

[23] Y. Ren, P. Liu, B. L. Zhou, X. Y. Zhou, and G. H. Zhou, Phys. Rev. Appl. **12**, 064025 (2019).

[24] J. Lu, Z. Q. Fan, J. Gong, J. Z. Chen, H. ManduLa, Y. Y. Zhang, S. Y. Yang, and X. W. Jiang, Phys. Chem. Chem. Phys. **20**, 5699 (2018).

[25] S. Liu, N. Huo, S. Gan, Y. Li, Z. Wei, B. Huang, J. Liu, J. Li, and H. Chen, J. Mater. Chem. C **3**, 10974 (2015).

[26] Y. P. An, Y. Hou, H. Wang, J. Li, R. Wu, T. Wang, H. Da, and J. Jiao, Phys. Rev. Appl. **11**, 064031 (2019).

[27] B. Z. Xu, M. S. Zhu, W. C. Zhang, X. Zhen, Z. X. Pei, Q. Xue, C. Y. Zhi, and P. Shi, Adv. Mater. **28**, 3333 (2016).

[28] B. Radisavljevic, A. Radenovic, J. Brivio, V. Giacometti, and A. Kis, Nat. Nanotechnol. **6**, 147 (2011).

[29] X. W. Jiang, J. Gong, N. Xu, S. S. Li, J. F. Zhang, Y. Hao, and L. W. Wang, Appl. Phys. Lett. **104**, 023512 (2014).

[30] Z. Q. Fan, Z. H. Zhang, and S. Y. Yang, Nanoscale **12**, 21750 (2020).

[31] X. F. Yan, Q. Chen, L. L. Li, H. Z. Guo, J. Z. Peng, and F. M. Peeters, Nano Energy **75**, 104953 (2020).

[32] C. Wang, X. C. Ren, C. H. Xu, B. B. Fu, R. H. Wang, X. T. Zhang, R. J. Li, H. X. Li, H. L. Dong, Y. G. Zhen, S. B. Lei, L. Jiang, and W. P. Hu, Adv. Mater. **30**, 1706260 (2018).

[33] Z. Q. Fan, X. W. Jiang, Z. M. Wei, J. W. Luo, and S. S. Li, J. Phys. Chem. C **121**, 14373 (2017).

[34] J. Zeng, K. Q. Chen, and Y. X. Tong, Carbon **127**, 611 (2018).

[35] R. Hu, Y. H. Li, Z. H. Zhang, Z. Q. Fan, and L. Sun, J. Mater. Chem. C **7**, 7745 (2019).

[36] J. Zhao, H. Zeng, and X. F. Zhou, Carbon **145**, 1 (2019).

[37] D. Sarkar, X. J. Xie, W. Liu, W. Cao, J. H. Kang, Y. J. Gong, S. Kraemer, P. M. Ajayan, and K. Banerjee, Nature **526**, 91 (2015).

[38] D. S. Schulman, A. J. Arnold, and S. Das, Chem. Soc. Rev. **47**, 3037 (2018).

[39] K. F. Mak, C. Lee, J. Hone, J. Shan, and T. F. Heinz, Phys. Rev. Lett. **105**, 136805 (2010).

[40] Q. H. Wang, K. Kalantar-Zadeh, A. Kis, J. N. Coleman, and M. S. Strano, Nat. Nanotechnol. **7**, 699 (2012).

[41] J. H. Kang, W. Liu, D. Sarkar, D. Jena, and K. Banerjee, Phys. Rev. X **4**, 031005 (2014).

[42] Y. Y. Wang, R. X. Yang, R. G. Quhe, H. X. Zhong, L. X. Cong, M. Ye, Z. Y. Ni, Z. G. Song, J. B. Yang, J. J. Shi, J. Li, and J. Lu, Nanoscale **8**, 1179 (2016).

[43] A. Ambrosi, Z. Sofer, and M. Pumera, Chem. Commun. **51**, 8450 (2015).

[44] X. Chia, A. Y. S. Eng, A. Ambrosi, S. M. Tan, and M. Pumera, Chem. Rev. **115**, 11941 (2015).

[45] H. Y. Jin, C. X. Guo, X. Liu, J. L. Liu, A. Vasileff, Y. Jiao, Y. Zheng, and S. Z. Qiao, Chem. Rev. **118**, 6337 (2018).

[46] H. H. Huang, X. F. Fan, D. J. Singh, and W. T. Zheng, Nanoscale **12**, 1247 (2020).

[47] R. Kappera, D. Voiry, S. E. Yalcin, B. Branch, G. Gupta, A. D. Mohite, and M. Chhowalla, Nat. Mater. **13**, 1128 (2014).

[48] Y. Q. Ma, B. L. Liu, A. Y. Zhang, L. Chen, M. Fathi, C. F. Shen, A. N. Abbas, M. Y. Ge, M. Mecklenburg, and C. W. Zhou, ACS Nano **9**, 7383 (2015).

[49] A. V. Kolobov, P. Fons, and J. Tominaga, Phys. Rev. B **94**, 094114 (2016).

[50] Z. Q. Fan, X. W. Jiang, J. W. Luo, L. Y. Jiao, R. Huang, S. S. Li, and L. W. Wang, Phys. Rev. B **96**, 165402 (2017).

[51] Z. Q. Fan, X. W. Jiang, J. Z. Chen, and J. W. Luo, ACS Appl. Mater. Interfaces **10**, 19271 (2018).

[52] H. Yang, J. Heo, S. Park, H. J. Song, D. H. Seo, K. E. Byun, P. Kim, I. Yoo, H. J. Chung, and K. Kim, Science **336**, 1140 (2012).

[53] Y. Katagiri, T. Nakamura, A. Ishii, C. Ohata, M. Hasegawa, S. Katsumoto, T. Cusati, A. Fortunelli, G. Iannaccone, G. Fiori, S. Roche, and J. Haruyama, Nano Lett. **16**, 3788 (2016).

[54] H. F. Huang, W. S. Xu, T. X. Chen, R. J. Chang, Y. W. Sheng, Q. Y. Zhang, L. L. Hou, and J. H. Warner, ACS Appl. Mater. Interfaces **10**, 37258 (2018).

[55] Y. P. An, Y. S. Hou, K. Wang, S. J. Gong, C. L. Ma, C. X. Zhao, T. X. Wang, Z. Y. Jiao, H. Y. Wang, and R. Q. Wu, Adv. Funct. Mater. **30**, 2002939 (2020).

[56] X. K. Chen and K. Q. Chen, J. Phys.: Condens. Matter **32**, 153002 (2020).

[57] Y. Xiao, Z. W. Wang, L. Shi, X. W. Jiang, S. S. Li, and L. W. Wang, Sci. China: Phys. Mech. Astron. **63**, 277312 (2020).

[58] S. Smidstrup, T. Markussen, P. Vancraeyveld, J. Wellendorff, J. Schneider, T. Gunst, B. Verstiche, D. Stradi, P. A. Khomyakov, U. G. Vej-Hansen, M. E. Lee, S. T. Chill, F. Rasmussen, G. Penazzi, F. Corsetti, A. Ojanper, K. Jensen, M. L. N. Palsgaard, U. Martinez, A. Blom *et al.*, J. Phys.: Condens. Matter **32**, 015901 (2020).

[59] M. Büttiker, Y. Imry, R. Landauer, and S. Pinhas, Phys. Rev. B **31**, 6207 (1985).

[60] Z. Q. Fan, J. Z. Chen, and X. W. Jiang, J. Phys. D: Appl. Phys. **51**, 335104 (2018).